

A battle of designs: triangular vs. L-shaped detectors and parity violation in the gravitational-wave background

Hannah Duval,^{1,*} Charles Badger,^{2,†} and Mairi Sakellariadou^{2,‡}

¹*Theoretische Natuurkunde, Vrije Universiteit Brussel, Pleinlaan 2, B-1050 Brussels, Belgium*

²*Theoretical Particle Physics and Cosmology Group, Physics Department,*

King's College London, University of London, Strand, London WC2R 2LS, United Kingdom

(Dated: February 26, 2026)

We investigate the prospects for detecting a parity-violating gravitational-wave background (GWB) with third-generation ground-based detector networks. We focus on a network consisting of one Einstein Telescope (ET) and two Cosmic Explorer (CE) detectors. In our analysis we vary the ET design, detector orientations, and arm lengths to assess the impact of geometry and scale on detection capabilities. We find that, among the configurations studied, networks with a 15 km triangular ET design provide the strongest parity-violation constraining power, followed by networks with an L-shaped ET design, while networks with 10 km triangular ET configurations are the least sensitive. Under current bounds, ET alone cannot confidently detect parity violation.

I. INTRODUCTION

The superposition of independent gravitational waves (GW) of cosmological and astrophysical origin forms a gravitational-wave background (GWB). The detection of such a background can shed light on early-universe mechanisms, such as inflation [1–3], first-order phase transitions [4–8], and cosmic strings [9–11], and aid in characterizing astrophysical compact binary coalescences (CBCs) sources and populations [12]. Searches for an unpolarized GWB using data from the ground-based interferometers LIGO [13] and Virgo [14] have placed upper limits on its energy density [15].

A multitude of mechanisms in the early universe can generate parity violation (PV) [16] that results in the production of asymmetric amounts of right- and left-handed circularly polarized GWs. Parity-violating sources and their effects on the GWB have been studied in the literature, including those arising from the Chern-Simons modification to gravity [17–19] and from axion inflation [20, 21], turbulence in the primordial plasma [22–24], or by primordial magnetic fields coupled to the cosmological plasma [25–29].

Probing for polarization in the GWB can place constraints on parity-violating theories [30]. Parity-violating effects in the GWB have been studied in the context of current and future detector sensitivities [31–39], and have been constrained through analyses of LIGO–Virgo data [30, 37, 40].

While PV detection appears unlikely in presently existing ground detectors, third-generation detectors show promise in detecting, or at least imposing tighter constraints in circular polarization. The choice of the detector network configuration will play a crucial role in the circular polarization detection prospects. In this study, we present a dual *theoretical* (based on signal-to-noise ratio) and *data-driven* (Bayesian) analysis for assessing the sensitivity of third-generation ground-based detector networks to parity-violating signatures in a general power-law GWB model.

II. FORMALISM

The right- and left-handed modes, defined through the circularly polarized bases $e^R = (e^+ + ie^\times)/\sqrt{2}$ and $e^L = (e^+ - ie^\times)/\sqrt{2}$ (with + and \times the plus and cross polarizations, respectively) read $h_R = (h_+ - ih_\times)/\sqrt{2}$ and $h_L = (h_+ + ih_\times)/\sqrt{2}$.

Right- and left-handed correlators are

$$\begin{aligned} & \begin{pmatrix} \langle h_R(f, \hat{\Omega}) h_R^*(f', \hat{\Omega}') \rangle \\ \langle h_L(f, \hat{\Omega}) h_L^*(f', \hat{\Omega}') \rangle \end{pmatrix} \\ &= \frac{\delta(f - f') \delta^2(\hat{\Omega} - \hat{\Omega}')}{4\pi} \begin{pmatrix} I(f, \hat{\Omega}) + V(f, \hat{\Omega}) \\ I(f, \hat{\Omega}) - V(f, \hat{\Omega}) \end{pmatrix}, \end{aligned} \quad (1)$$

where $\langle \cdot \rangle$ is the ensemble average and I, V are the Stokes parameters; V characterizes the asymmetry between right- and left-handed polarized waves, and $I (\geq |V|)$ is the gravitational wave's total amplitude. The polarization degree $\Pi(f) = V(f)/I(f) \in [-1, 1]$, with $\Pi = -1$ and $\Pi = +1$ defining fully left- and right-handed polarization, respectively, while $\Pi = 0$ stands for an unpolarized isotropic GWB. For the latter ($V = 0$), Eq. (1) reduces to the standard correlator for an unpolarized isotropic background. The signal-to-noise ratios (SNRs) ρ_I and ρ_V for the I - and V -modes, respectively, of a circularly polarized GWB, are calculated for a detector network over an observing time T [41]. The power-law integrated (PI) curve, $\Omega_{PI,I}$, characterizes a detector network's I -mode sensitivity [42]. We extend the procedure to the V -mode to obtain the PI sensitivity curve, $\Omega_{PI,V}$, for the V -mode.

To search for parity-violating GWBs, we adapt the formalism described in [41, 43] to third-generation ground-based detector networks.

III. PARITY VIOLATING MODELS

We explore the parity-violation detection prospects of the modified GWB spectrum from formalism [30, 43]

$$\Omega'_{GW}(f) = \Omega_{GW}(f) \left[1 + \Pi(f) \frac{\gamma_V^{d_1 d_2}(f)}{\gamma_I^{d_1 d_2}(f)} \right], \quad (2)$$

* Hannah.Marie.D.Duval@vub.be

† charles.badger@kcl.ac.uk

‡ mairi.sakellariadou@kcl.ac.uk

as it would appear in the detector pairs d_1, d_2 where $\gamma_{I/V}^{d_1 d_2}$ are the normalized overlap reduction functions for the I - and V -modes calculated via analytical and numerical methods [44, 45] defined as the usual

$$\gamma_{I}^{d_1 d_2}(f) = \frac{5}{8\pi} \int d\hat{\Omega} (F_{d_1}^+ F_{d_2}^{+*} + F_{d_1}^\times F_{d_2}^{\times*}) e^{2\pi i f \hat{\Omega} \Delta \vec{x}}, \quad (3)$$

$$\gamma_{V}^{d_1 d_2}(f) = -\frac{5i}{8\pi} \int d\hat{\Omega} (F_{d_1}^+ F_{d_2}^{\times*} - F_{d_1}^\times F_{d_2}^{+*}) e^{2\pi i f \hat{\Omega} \Delta \vec{x}}, \quad (4)$$

for beam pattern function F_d^A for the usual $A = +, \times$ polarizations.

We assume a general power-law GWB spectrum $\Omega_{\text{GW}} = \Omega_\alpha (f/f_{\text{ref}})^\alpha$ parametrized by amplitude Ω_α and spectral index α [37]; we set the reference frequency $f_{\text{ref}} = 25$ Hz. Theoretically motivated polarized GWBs can be modeled by specific choices of α , with the polarization typically assumed constant for simplicity. For instance, GWBs sourced by non-Abelian axion inflation [3, 46], string-inspired cosmology models [17], and some turbulence models [47] can be well-modeled by a power-law GWB with constant polarization. In what follows, we adopt this assumption, $\Pi(f) = \text{const}$, noting that the framework can be generalized to arbitrary polarized GWBs, for example, a frequency-dependent power-law $\Pi(f)$ model [37].

IV. FUTURE GROUND-BASED DETECTOR CONFIGURATIONS

We consider seven representative networks, each combining one Einstein Telescope (ET) with two Cosmic Explorer (CE) detectors, using the geometric information from [48]. We include triangular ET designs with 10 and 15 km arms (Δ_{10}, Δ_{15}), as well as ET designs consisting of two L-shaped detectors with 15 km arms (S, R), following the standard ET configurations introduced in [49] and extended to ET+CE networks in [48]. For CE, we consider L-shaped detectors with 20 km (P) and 40 km (Y) arms. The triangular configurations consist of three detectors, while an L-shaped configuration consists of one. Thus a $\Delta + (\text{PY})$ network contains five detectors (10 baselines), while an (SR) + (PY) network contains four (6 baselines). These configurations explore how detector orientations and arm length influence network performance, with some optimized for GWB sensitivity and others for CBC source localization, clarifying whether differences between triangular and L-shaped designs arise from geometry or arm length. Further technical details are in [48], for which we use the amplitude spectral density curves found in [50] and [51], and the full set of configuration names and descriptions is in Table I.

In Fig. 1, we present the I - and V -mode PI curves for the various network configurations, extending previous ET design studies [49] to networks combining ET with CE and to V -mode sensitivity. The $\Omega_{\text{PI}, I}$ curves show that GWB-optimized networks yield the highest I -mode sensitivity, which is expected by construction. In particular, (SR)₁(PY)₁ dominates

Network name	Description
$\Delta_{10}(\text{PY})_4$	10 km Δ + 2CE, GWB-optimized
$\Delta_{10}(\text{PY})_5$	10 km Δ + 2CE, Localization-optimized
$\Delta_{15}(\text{PY})_4$	15 km Δ + 2CE, GWB-optimized
$\Delta_{15}(\text{PY})_5$	15 km Δ + 2CE, Localization-optimized
(SR) ₁ (PY) ₁	15 km 2L + 2CE, GWB-optimized
(SR) ₂ (PY) ₂	15 km 2L + 2CE, Localization-optimized
(SR) ₃ (PY) ₃	15 km 2L + 2CE, Hybrid

TABLE I: The different third-generation detector network configurations that are considered in this study, which follow the definitions and optimization procedures of [48].

“GWB-optimized” denotes configurations favoring GWB sensitivity and are determined using a PI-curve method, while “Localization-optimized” configurations favor source localization and are computed using the network-alignment factor. “Hybrid” configurations provide a balanced design providing a trade-off between the two.

below 20 Hz, while at higher frequencies all triangular configurations outperform the 2L designs.

The $\Omega_{\text{PI}, V}$ curves exhibit reduced sensitivity compared to their I -mode counterparts, with sensitivity decreasing as $|\Pi|$ approaches 0. Their ranking is relatively stable across frequencies: $\Delta_{15}(\text{PY})_4$ is consistently the most sensitive configuration, while $\Delta_{10}(\text{PY})_5$ performs the worst. Overall, networks incorporating a 15 km triangular ET design achieve the highest sensitivity to V -modes, followed by 2L ET networks, whereas 10 km triangular ET configurations are the least sensitive. The superior performance of the 15 km triangular configuration relative to the 15 km 2L case arises from its larger number of independent baselines. In the 10 km triangular configuration, however, higher instrumental noise dominates, leading to reduced sensitivity. Sensitivity to V -modes is therefore controlled by a combination of arm length, the number of independent baselines, and network geometry. The parity-violation detection prospects of ET alone are presented in Appendix A. We find that current constraints [40] have already excluded the parameter space in which ET alone would be capable of detecting circular polarization. Therefore, the inclusion of CE detectors is a necessity to make robust parity-violation inferences.

V. FUTURE DETECTION PROSPECTS

We present *theoretical* (based on signal-to-noise ratio) and *data-driven* (obtained with a Bayesian analysis) prospects for detecting PV by applying the previously described formalisms to third-generation detector networks. Our analysis covers general power-law GWBs with $-12.5 \leq \log_{10} \Omega_\alpha \leq -10$, spectral indices $\alpha = -3, \dots, 3$, and polarization degrees $-1 \leq \Pi \leq 1$. We note that the upper bound on the $\log_{10} \Omega_\alpha$ range is determined by current detector constraints [15], while the lower bound is to allow studied GWBs to be potentially detected in the considered networks, as seen in Fig. 1.

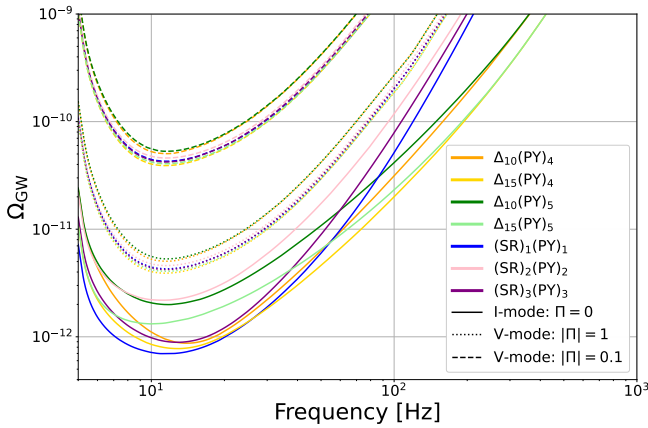


FIG. 1: PI sensitivity curves for I -mode (solid lines) and V -mode (dotted and dashed lines), shown for the seven different detector third-generation network configurations for an observing time of one year and $\rho = 4$. The V -mode curves correspond to $|\Pi| = 1$ (dotted) and $|\Pi| = 0.1$ (dashed).

A. Signal-to-noise ratio

The sensitivities of the third-generation detector networks are quantified by the I - and V -mode SNRs. Fig. 2 shows the results for a flat PL ($\alpha = 0$) spectrum across the seven network configurations. As expected, ρ_I is independent of Π and scales only with the GWB amplitude, while ρ_V grows with $|\Pi|$, enhancing detectability for more strongly polarized backgrounds. We repeat this study for other power-law indices and rank their detection prospects in Tables II and III.

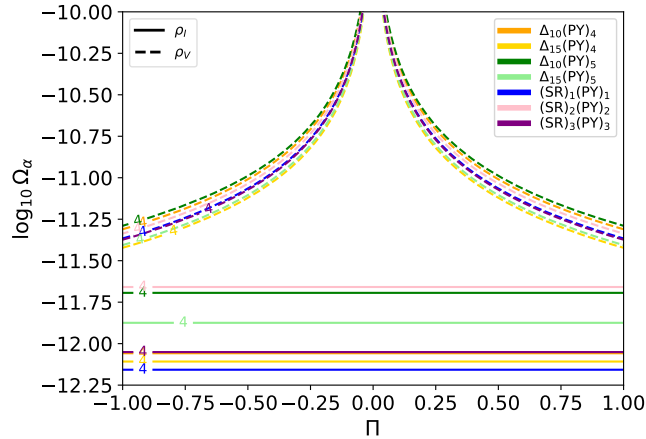


FIG. 2: SNRs for I -mode (solid lines) and V -mode (dashed lines) for the seven third-generation detector network configurations, assuming a flat ($\alpha = 0$) power-law GWB.

We find that the 2L network $(\text{SR})_1(\text{PY})_1$ provides the largest ρ_I for $-3 \leq \alpha \leq 1$, while the 15 km triangular network $\Delta_{15}(\text{PY})_4$ overtakes it at $\alpha = 2$, highlighting the advantage of a triangular design for GWBs with large positive spectral indices. For the V -mode, $\Delta_{15}(\text{PY})_4$ is the most sensitive

Order	α	$-3, -2$	$-1, 0, \frac{1}{3}, \frac{1}{2}, \frac{2}{3}, 1$	2	3
1st		$(\text{SR})_1(\text{PY})_1$	$(\text{SR})_1(\text{PY})_1$	$\Delta_{15}(\text{PY})_4$	$\Delta_{15}(\text{PY})_4$ $\Delta_{15}(\text{PY})_5$
2nd		$\Delta_{15}(\text{PY})_4$	$\Delta_{15}(\text{PY})_4$	$(\text{SR})_1(\text{PY})_1$	$\Delta_{10}(\text{PY})_4$ $\Delta_{10}(\text{PY})_5$
3rd		$\Delta_{15}(\text{PY})_5$	$(\text{SR})_3(\text{PY})_3$	$\Delta_{15}(\text{PY})_5$	$(\text{SR})_1(\text{PY})_1$
4th		$(\text{SR})_3(\text{PY})_3$	$\Delta_{10}(\text{PY})_4$	$\Delta_{10}(\text{PY})_4$	$(\text{SR})_3(\text{PY})_3$
5th		$\Delta_{10}(\text{PY})_4$	$\Delta_{15}(\text{PY})_5$	$(\text{SR})_3(\text{PY})_3$	$(\text{SR})_2(\text{PY})_2$
6th		$(\text{SR})_2(\text{PY})_2$	$\Delta_{10}(\text{PY})_5$	$\Delta_{10}(\text{PY})_5$	
7th		$\Delta_{10}(\text{PY})_5$	$(\text{SR})_2(\text{PY})_2$	$(\text{SR})_2(\text{PY})_2$	

TABLE II: Ranking from best (1st) to worst (7th) of detector networks by I -mode SNRs for different PL indices α , grouping together indices that yield identical prospects.

Order	α	-3 to 1	2, 3
1st		$\Delta_{15}(\text{PY})_4$	$\Delta_{15}(\text{PY})_4$
2nd		$\Delta_{15}(\text{PY})_5$	$\Delta_{15}(\text{PY})_5$
3rd		$(\text{SR})_3(\text{PY})_3$	$(\text{SR})_1(\text{PY})_1$
4th		$(\text{SR})_1(\text{PY})_1$	$(\text{SR})_3(\text{PY})_3$
5th		$(\text{SR})_2(\text{PY})_2$	$(\text{SR})_2(\text{PY})_2$
6th		$\Delta_{10}(\text{PY})_4$	$\Delta_{10}(\text{PY})_4$
7th		$\Delta_{10}(\text{PY})_5$	$\Delta_{10}(\text{PY})_5$

TABLE III: Ranking from best (1st) to worst (7th) of detector networks by V -mode SNRs for different PL indices α .

configuration across all α values, with the 2L networks consistently outperforming the 10 km triangular configurations. This hierarchy indicates that optimal parity-violation detection is achieved with a 15 km triangular ET combined with two CEs. This behavior is consistent with the PI curves in Fig. 1, whose frequency-dependent shapes qualitatively explain the SNR rankings across different spectral indices. We highlight that fixing different reference frequencies yields the same ordering of SNR prospects, emphasizing the generality of our results. Appendix A presents ET-only configurations and shows that all triangular ET designs suffer a dramatic loss of PV sensitivity compared to 2L designs.

B. Bayesian analysis

We now complement the SNR analysis with a data-driven Bayesian analysis on simulated signals, assuming the design sensitivity and noise characteristics of each third-generation network configuration. Parameter estimation is carried out with the `pygwb` [52] and `Bilby` [53] packages using the `Dynesty` sampler. This allows us to assess a network's capability to detect a polarized signal and to distinguish it from an unpolarized one. To this end, we fix a power-law index α and generate 1600 simulated injections uniformly over the $\log_{10} \Omega_\alpha$ and Π range in each network configuration, then searching over the priors of Table IV based off of theoretical bounds and previously explored search priors [40, 54]. The procedure is then repeated with $\Pi = 0$ to model unpolarized backgrounds, using the same amplitude and spectral index pri-

ors. To reduce statistical noise, we generate 15 independent injection sets with random detector noise and combine results with an optimized weighted average [44]. This enables a direct comparison between polarized and unpolarized searches.

Parameters θ	Priors
$\log_{10} \Omega_\alpha$	Uniform(-18, -7)
α	Gaussian(0, 3.5)
Π	Uniform(-1, 1)

TABLE IV: Priors used in the Bayesian analysis. The $\log_{10} \Omega_\alpha$ and α priors follow previous searches, while taking into account the sensitivity of third-generation detectors [54, 55]. The prior on Π is the full, physically allowed range of values [37].

1. Comparison to signal-to-noise

We compare the recovered data-analysis Bayes factors to the I - and V -mode SNRs for all injections. Fig. 3 shows this comparison for the $(\text{SR})_3(\text{PY})_3$ and $\Delta_{10}(\text{PY})_5$ configurations for a flat GWB spectrum. More concretely, it shows the SNRs alongside the log Bayes factors for a polarized model compared to detector noise, $\ln \mathcal{B}_{\text{Noise}}^{\Pi \neq 0}$, and to an unpolarized model, $\ln \mathcal{B}_{\text{Noise}}^{\Pi = 0}$. We adopt strong detection thresholds of $\ln \mathcal{B}_{\text{Noise}}^{\Pi \neq 0}$ and $\ln \mathcal{B}_{\text{Noise}}^{\Pi = 0}$ equal to 8. These correspond to ρ_I and ρ_V equal to 4, since $\rho^2 \simeq 2 \ln \mathcal{B}$ in the strong signal regime [44]. Our findings confirm this relation. In conclusion, the SNR predictions reproduce the trends seen in the data-driven analysis across both networks, demonstrating that simple theoretical estimates based on SNRs provide an excellent guide to the detectability of polarized GWBs. We note that the present analysis assumes uncorrelated detector noise. For the ET triangular configuration, correlated Newtonian noise between the co-located detectors is expected to further degrade the sensitivity to GWBs [56]. Since such correlated noise is absent for spatially separated L-shaped detectors, including this effect would reduce the performance of the triangular network and strengthen the preference for 2L configurations found here.

2. Parameter estimation

We perform a Bayesian analysis to assess parameter recovery of simulated parity-violating GWBs for the $(\text{SR})_3(\text{PY})_3$ and $\Delta_{10}(\text{PY})_5$ configurations. From the marginalized posteriors, we compute the 95% Upper Limits (UL) and Lower Limits (LL) on Π , allowing us to make $\Pi = 0$ exclusion analyses. This is shown in Fig. 3: purple and green regions denote where $\Pi = 0$ is ruled out with at least 95% confidence by the 2L and triangular networks, respectively. We define a threshold region as the parameter space where the 2L network excludes $\Pi = 0$ at 95% confidence, but the triangle network

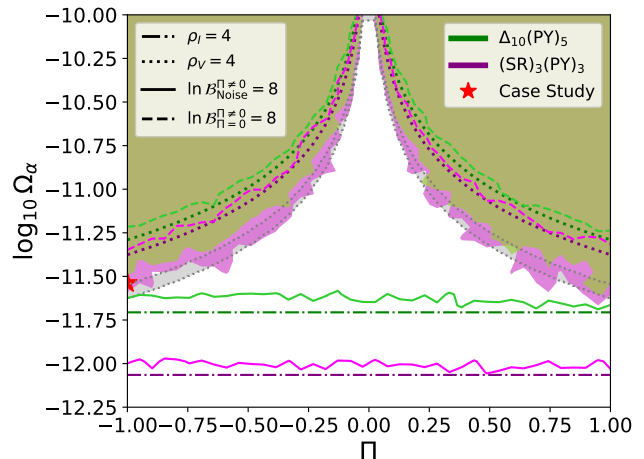


FIG. 3: SNR and log Bayes detection prospects for I - and V -modes in a flat GWB in the $\Delta_{10}(\text{PY})_5$ and $(\text{SR})_3(\text{PY})_3$ configurations. The green and purple filled regions correspond to 95% exclusion regions of $\Pi = 0$. The gray-shaded region indicates where $\rho_V^{\Delta_{10}(\text{PY})_5} \leq \rho_V^{95\%, \text{crit}} \leq \rho_V^{(\text{SR})_3(\text{PY})_3}$, where $\rho_V^{95\%, \text{crit}} = 2.16$ is the approximate V -mode SNR where $\Pi = 0$ is excluded at 95%. The red star marks the case study discussed in Sec. V B 2.

does not. An average V -mode SNR corresponding to the borders of this threshold region is $\rho_V^{\Delta_{10}(\text{PY})_5} \leq 2.16 \leq \rho_V^{(\text{SR})_3(\text{PY})_3}$, which is indicated by the gray-shaded region in Fig. 3.

Next, we focus on a flat parity-violating GWB case study with $\log_{10} \Omega_\alpha = -11.54$, $\Pi = -1$, indicated by the red star in Fig. 3. These parameters were chosen so that the signal lies in the threshold regime. The combined posterior results are shown in Fig. 4, where model parameters are recovered within 1σ for both networks. We derive the 95% UL on Π equal to -0.238 and 0.233 for the 2L and triangular network, respectively. We also compute log Bayes factors for the parity-violating and the unpolarized GWB searches. For the $(\text{SR})_3(\text{PY})_3$ network, we obtain $\ln \mathcal{B}_{\text{Noise}}^{\Pi \neq 0} = 2.914 \pm 0.043$, while for $\Delta_{10}(\text{PY})_5$ we find $\ln \mathcal{B}_{\text{Noise}}^{\Pi \neq 0} = 0.946 \pm 0.037$, highlighting the greater capability of $(\text{SR})_3(\text{PY})_3$ to distinguish a polarized from unpolarized GWBs than $\Delta_{10}(\text{PY})_5$. Although these log Bayes factors do not indicate a strong preference for a PV model, this injection demonstrates that $(\text{SR})_3(\text{PY})_3$ can rule out $\Pi = 0$ at the 95% confidence level, while $\Delta_{10}(\text{PY})_5$ cannot.

In conclusion, these findings highlight that network design strongly impacts parameter constraints, particularly for circular polarization Π , with $(\text{SR})_3(\text{PY})_3$ providing tighter constraints on parity-violating GWBs than $\Delta_{10}(\text{PY})_5$.

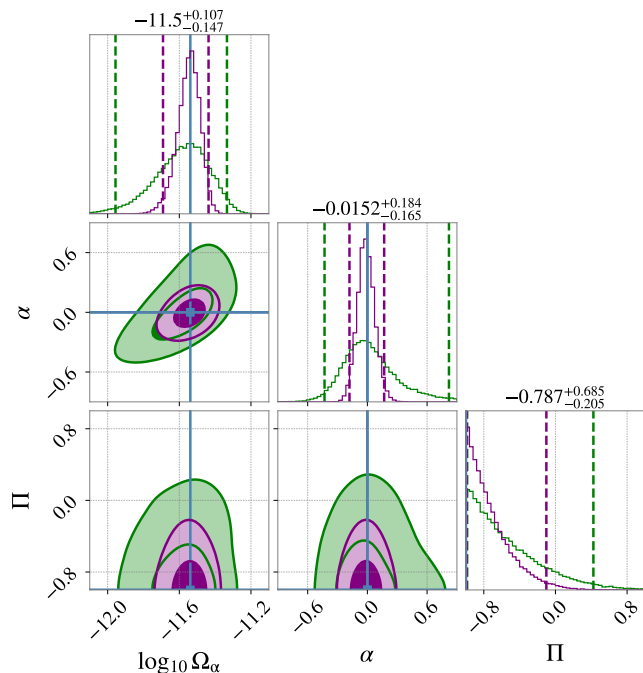


FIG. 4: Posterior distributions from Bayesian inference for parity-violating power-law GWBs, combined over 15 simulated runs for $f_{\text{ref}} = 25$ Hz. Shown are the $(\text{SR})_3(\text{PY})_3$ (purple) and $\Delta_{10}(\text{PY})_5$ (green) networks, with dark and light shading indicating 1σ and 2σ credible regions. Here: $\Pi = -1$ and $\log_{10} \Omega_\alpha = -11.54$ shown in blue.

VI. CONCLUSIONS

In this study, the detection prospects of a general parity-violating GWB with third-generation detector networks were investigated using a signal-to-noise ratio and a Bayesian analysis approach. By extending the standard GWB formalism to include the V -mode, we introduced PI curves and SNR prospects that accurately reproduce data-based results, providing an efficient proxy for assessing circular polarization detection prospects.

We considered an ET detector, in both triangular and 2L designs, paired with two CE detectors across a range of orientations, and ET arm lengths. A broad set of power-law GWB spectra, motivated by cosmological parity-violating mechanisms, was analyzed.

Across all scenarios, 15 km triangular ET configurations are most sensitive to parity violation, followed by 2L configurations, while 10 km triangular ET configurations are the least sensitive. Parameter estimation studies further demonstrate that network design strongly affects the ability to constrain the GWB parameters. We find that adopting a more sensitive network configuration can tighten the searched parameter space and can place polarization bounds that exclude $\Pi = 0$ at 95% compared to less sensitive detector designs. In Appendix A, we show that parity violation detection in ET alone has been ruled out; circular polarization in a third-generation network requires CE detectors.

These findings underscore the importance of a global network design choices in order to optimize the discovery potential for fundamental physics in the GWB. These results highlight how next-generation detectors could open a direct observational window onto fundamental parity-violating physics in the early Universe.

ACKNOWLEDGMENTS

We are grateful to Jacopo Uggeri for extensive discussions. We also thank Michael Ebersold for valuable insights on third-generation network configurations, Alberto Mariotti and Miguel Vanvlasselaer for helpful discussions, and Gianmassimo Tasinato and Angelo Ricciardone for useful comments. This document has an ET document number ET-0483A-25. The work of MS is partially supported by the Science and Technology Facilities Council (STFC grant ST/X000753/1). HD is supported by the Strategic Research Program High-Energy Physics of the Research Council of the Vrije Universiteit Brussel, the iBOF “Unlocking the Dark Universe with Gravitational Wave Observations: from Quantum Optics to Quantum Gravity” of the Vlaamse Interuniversitaire Raad.

- [1] L. P. Grishchuk, *Zh. Eksp. Teor. Fiz.* **67**, 825 (1974).
- [2] A. A. Starobinsky, *JETP Lett.* **30**, 682 (1979).
- [3] C. Badger, H. Duval, T. Fujita, S. Kuroyanagi, A. Romero-Rodríguez, and M. Sakellariadou, *Phys. Rev. D* **110**, 084063 (2024), arXiv:2406.11742 [astro-ph.CO].
- [4] M. Kamionkowski, A. Kosowsky, and M. S. Turner, *Phys. Rev. D* **49**, 2837 (1994), arXiv:astro-ph/9310044.
- [5] R. Apreda, M. Maggiore, A. Nicolis, and A. Riotto, *Nucl. Phys. B* **631**, 342 (2002), arXiv:gr-qc/0107033.
- [6] C. Grojean and G. Servant, *Phys. Rev. D* **75**, 043507 (2007), arXiv:hep-ph/0607107.
- [7] A. Romero, K. Martinovic, T. A. Callister, H.-K. Guo, M. Martínez, M. Sakellariadou, F.-W. Yang, and Y. Zhao, *Phys. Rev. Lett.* **126**, 151301 (2021), arXiv:2102.01714 [hep-ph].
- [8] C. Badger et al., *Phys. Rev. D* **107**, 023511 (2023), arXiv:2209.14707 [hep-ph].
- [9] P. Auclair et al., *JCAP* **04**, 034 (2020), arXiv:1909.00819 [astro-ph.CO].
- [10] T. Damour and A. Vilenkin, *Phys. Rev. D* **64**, 064008 (2001), arXiv:gr-qc/0104026.
- [11] R. Abbott et al. (LIGO Scientific, Virgo, KAGRA), *Phys. Rev. Lett.* **126**, 241102 (2021), arXiv:2101.12248 [gr-qc].
- [12] R. Abbott et al. (KAGRA, VIRGO, LIGO Scientific), *Phys. Rev. X* **13**, 011048 (2023), arXiv:2111.03634 [astro-ph.HE].
- [13] J. Aasi et al. (LIGO Scientific), *Class. Quant. Grav.* **32**, 074001 (2015), arXiv:1411.4547 [gr-qc].
- [14] F. Acernese et al. (VIRGO), *Class. Quant. Grav.* **32**, 024001 (2015), arXiv:1408.3978 [gr-qc].
- [15] A. G. Abac et al. (LIGO Scientific, VIRGO, KAGRA), (2025), arXiv:2508.20721 [gr-qc].
- [16] S. H. S. Alexander, M. E. Peskin, and M. M. Sheikh-Jabbari, *Physical Review Letters* **96** (2006), 10.1103/physrevlett.96.081301.
- [17] M. Satoh, S. Kanno, and J. Soda, *Physical Review D* **77** (2008), 10.1103/physrevd.77.023526.
- [18] N. Bartolo, L. Caloni, G. Orlando, and A. Ricciardone, *Journal of Cosmology and Astroparticle Physics* **2021**, 073 (2021).
- [19] T. Takahashi and J. Soda, *Phys. Rev. Lett.* **102**, 231301 (2009).
- [20] N. Barnaby and M. Peloso, *Physical Review Letters* **106** (2011), 10.1103/physrevlett.106.181301.
- [21] E. Dimastrogiovanni and M. Peloso, *Physical Review D* **87** (2013), 10.1103/physrevd.87.103501.
- [22] M. Kamionkowski, A. Kosowsky, and M. S. Turner, *Physical Review D* **49**, 2837–2851 (1994).
- [23] E. Witten, *Phys. Rev. D* **30**, 272 (1984).
- [24] C. J. Hogan, *MNRAS* **218**, 629 (1986).
- [25] A. Brandenburg, K. Enqvist, and P. Olesen, *Physical Review D* **54**, 1291–1300 (1996).
- [26] M. Christensson, M. Hindmarsh, and A. Brandenburg, *Physical Review E* **64** (2001), 10.1103/physreve.64.056405.
- [27] T. Kahniashvili, A. Brandenburg, A. G. Tevzadze, and B. Ratra, *Physical Review D* **81** (2010), 10.1103/physrevd.81.123002.
- [28] A. Brandenburg, T. Kahniashvili, S. Mandal, A. R. Pol, A. G. Tevzadze, and T. Vachaspati, *Physical Review Fluids* **4** (2019), 10.1103/physrevfluids.4.024608.
- [29] A. Brandenburg, Y. He, T. Kahniashvili, M. Rheinhardt, and J. Schober, (2021), arXiv:2101.08178 [astro-ph.CO].
- [30] S. Crowder, R. Namba, V. Mandic, S. Mukohyama, and M. Peloso, *Physics Letters B* **726**, 66–71 (2013).
- [31] N. Seto, *Phys. Rev. D* **75**, 061302 (2007).
- [32] A. Ricciardone, *Journal of Physics: Conference Series* **840**, 012030 (2017).
- [33] G. Orlando, M. Pieroni, and A. Ricciardone, *Journal of Cosmology and Astroparticle Physics* **2021**, 069 (2021).
- [34] N. Bartolo, V. Domcke, D. G. Figueroa, J. García-Bellido, M. Peloso, M. Pieroni, A. Ricciardone, M. Sakellariadou, L. Sorbo, and G. Tasinato, *JCAP* **11**, 034 (2018), arXiv:1806.02819 [astro-ph.CO].
- [35] V. Domcke, J. García-Bellido, M. Peloso, M. Pieroni, A. Ricciardone, L. Sorbo, and G. Tasinato, *Journal of Cosmology and Astroparticle Physics* **2020**, 028–028 (2020).
- [36] P. Xu, Z. Wang, and L.-E. Qiang, *Physics Letters B* **789**, 378 (2019).
- [37] K. Martinovic, C. Badger, M. Sakellariadou, and V. Mandic, *Phys. Rev. D* **104**, L081101 (2021), arXiv:2103.06718 [gr-qc].
- [38] C. Badger and M. Sakellariadou, (2021), arXiv:2112.04650 [gr-qc].
- [39] N. M. J. Cruz, A. Malhotra, G. Tasinato, and I. Zavala, *Phys. Rev. D* **110**, 103505 (2024), arXiv:2406.04957 [astro-ph.CO].
- [40] A. G. Abac et al. (LIGO Scientific, VIRGO, KAGRA), (2025), arXiv:2510.26848 [gr-qc].
- [41] N. Seto and A. Taruya, *Phys. Rev. D* **77**, 103001 (2008), arXiv:0801.4185 [astro-ph].
- [42] E. Thrane and J. D. Romano, *Phys. Rev. D* **88**, 124032 (2013), arXiv:1310.5300 [astro-ph.IM].
- [43] N. Seto and A. Taruya, *Phys. Rev. Lett.* **99**, 121101 (2007).
- [44] J. D. Romano and N. J. Cornish, *Living Reviews in Relativity* **20** (2017), 10.1007/s41114-017-0004-1.
- [45] I. Caporali and A. Ricciardone, (2025), arXiv:2507.15791 [astro-ph.IM].
- [46] A. Maleknejad, *JHEP* **07**, 104 (2016), arXiv:1604.03327 [hep-ph].
- [47] T. Kahniashvili, G. Gogoberidze, and B. Ratra, *Physical Review Letters* **95** (2005), 10.1103/physrevlett.95.151301.
- [48] M. Ebersold, T. Regimbau, and N. Christensen, *Phys. Rev. D* **110**, 122006 (2024), arXiv:2408.06032 [gr-qc].
- [49] M. Branchesi et al., *JCAP* **07**, 068 (2023), arXiv:2303.15923 [gr-qc].
- [50] S. Danilishin and T. Zhang, “ET sensitivity curves used for CoBA science study,” (2023).
- [51] P. Fulda, L. Barsotti, M. Evans, and K. Kuns, *CE Document T2000017-v8* (2023).
- [52] A. I. Renzini et al., *J. Open Source Softw.* **9**, 5454 (2024).
- [53] G. Ashton et al., *Astrophys. J. Suppl.* **241**, 27 (2019), arXiv:1811.02042 [astro-ph.IM].
- [54] K. Martinovic, P. M. Meyers, M. Sakellariadou, and N. Christensen, *Phys. Rev. D* **103**, 043023 (2021), arXiv:2011.05697 [gr-qc].
- [55] R. Abbott, T. D. Abbott, S. Abraham, F. Acernese, K. Ackley, A. Adams, C. Adams, R. X. Adhikari, V. B. Adya, C. Affeldt, D. Agarwal, and et. al. (LIGO Scientific Collaboration, Virgo Collaboration, and KAGRA Collaboration), *Phys. Rev. D* **104**, 022004 (2021).
- [56] K. Janssens et al., *Phys. Rev. D* **109**, 102002 (2024), arXiv:2402.17320 [gr-qc].

Appendix A: Discussion on Einstein Telescope alone

We briefly assess the detection prospects of a parity violating GWB using ET alone, building on previous ET-only detector design and sensitivity studies [49]. For this purpose, we consider baselines that differ from those adopted in the main analysis. Specifically, we introduce the notation Δ'_{10} and Δ'_{15} to denote closed, fully symmetric triangular ET configurations with 10 km and 15 km arms, respectively. These correspond to the idealized case of a perfectly equilateral triangle formed by three co-located detectors, with each vertex separated by 60° . For comparison, we also include the configurations Δ_{10} and Δ_{15} already used in the main text and defined in [48]. These differ in that the three detectors do not form an exactly closed triangle. As a result, the Δ_{10} and Δ_{15} configurations are slightly asymmetric. This asymmetry yields enhanced sensitivity to V -modes, since the chiral ORF is slightly larger than that of a perfectly closed triangle.

In addition to triangular configurations, we also examine two 2L configurations, denoted by $(SR)_0$ and $(SR)_{45}$. The $(SR)_0$ setup corresponds to the optimal 2L configuration for GWB detection where the two detectors are aligned (relative orientation of 0°). By contrast, the $(SR)_{45}$ represents the most pessimistic case for GWB detection, where the detectors are rotated by 45° with respect to one another, consistent with previous studies of 2L configurations and relative orientations [49]). It is important to emphasize that $(SR)_0$ and $(SR)_{45}$ differ from $(SR)_1$ and $(SR)_2$ considered in the main analysis, since the latter were defined relative to the optimal configuration of a global network including two CEs, whereas here the reference is ET alone. In Table V, the latitude and longitude of each network center, the X- and Y-arm endpoints and azimuths are given.

Fig. 5 shows the PI curves for both the I - and V -modes across the different ET-only configurations. For the I -mode sensitivities, the trends are consistent with previous ET-only sensitivity studies [49], while here we additionally present the corresponding V -mode sensitivities relevant for parity-violating GWBs. For comparison, we also include a parity-violating PL GWB with spectral index $\alpha = 0$, to facilitate direct comparison with the corresponding SNR prospects shown in Fig. 6. The perfectly closed and symmetric triangular configurations Δ' exhibit noticeably lower V -mode sensitivity than the slightly asymmetric Δ setups used in the main text, illustrating that even small asymmetries in ET's geometry can enhance parity-violation detection. Nevertheless, all triangular configurations, whether symmetric or slightly asymmetric, are significantly less sensitive to the V -modes than the 2L designs.

We have again performed SNR studies for multiple spectral indices α . For the I -mode SNRs, the ranking from most to least sensitive is: $(SR)_0$, $(SR)_{45}$, $\Delta_{15} = \Delta'_{15}$ and $\Delta_{10} = \Delta'_{10}$. For the V -mode SNRs, the resulting network rankings are summarized in Tables VI, confirming that 2L configurations consistently outperform triangular ET for V -mode detection. We note that correlated Newtonian noise between the co-located detectors of the triangular configuration [56] is not in-

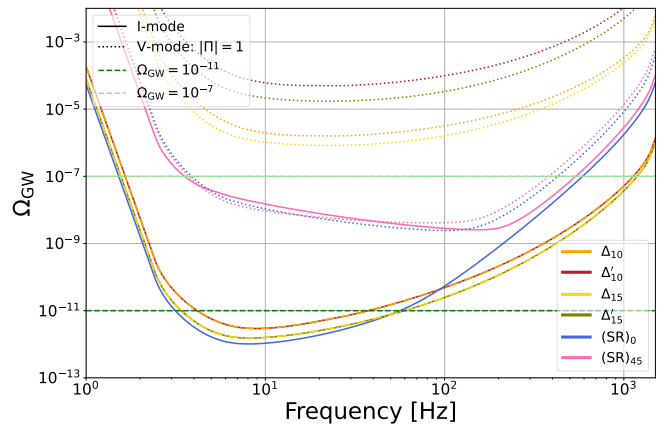


FIG. 5: PI curves sensitivity curves for I -mode (solid lines) and V -mode (dotted and dashed lines), shown for the 6 different ET configurations, for an observing time of one year and $\rho = 4$. The V -mode curves correspond to $|\Pi| = 1$ (dotted) and $|\Pi| = 0.1$ (dashed). We also show PL GWBs with spectral index of $\alpha = 0$.

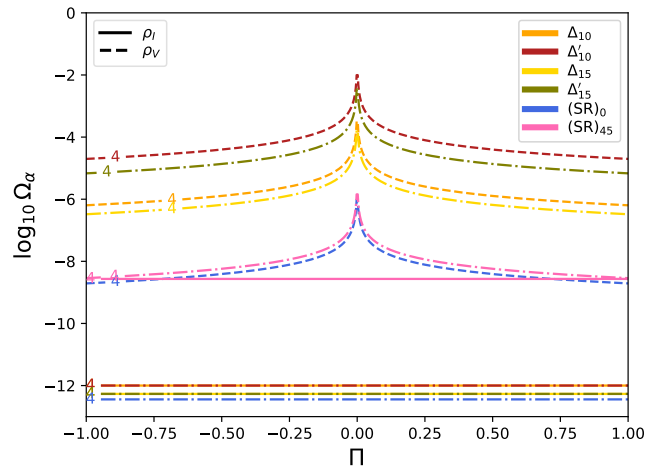


FIG. 6: SNRs for I -mode (solid lines) and V -mode (dashed lines), shown for the five different ET configurations for a PL GWB with $\alpha = 0$.

cluded in the present study. Accounting for this contribution would further reduce the sensitivity prospects of the triangular ET designs. Moreover, current bounds on the parity-violated GWB [40] have ruled out the parity-violating parameter space that is detectable by both 2L and the Δ configurations, as seen in Fig. 6. Consequently, if ET were constructed without CE, none of the configurations would be able to detect circularly polarized GWBs at a confident SNR level.

Name	Origin (lat, lon)	X-arm end (lat, lon)	Y-arm end (lat, lon)	Azimuth [°] X-/Y-arm
E1' ₁₀	43.6300, 10.5000	43.7149, 10.5413	43.6983, 10.4193	19.43 /319.43
E2' ₁₀	43.7149, 10.5413	43.6983, 10.4193	43.6300, 10.5000	259.46 /199.46
E3' ₁₀	43.6983, 10.4193	43.6300, 10.5000	43.7149, 10.5413	139.37 /79.37
E1' ₁₅	43.6300, 10.5000	43.7573, 10.5620	43.7325, 10.3789	19.43 /319.43
E2' ₁₅	43.7573, 10.5620	43.7325, 10.3789	43.6300, 10.5000	259.47 /199.47
E3' ₁₅	43.7325, 10.3789	43.6300, 10.5000	43.75730, 10.5620	139.35/79.35
S ₀	40.5200, 9.4170	40.3851, 9.4093	40.5258, 9.2402	182.51/272.51
S ₄₅	40.5200, 9.4170	40.4203, 9.5364	40.4287, 9.2867	137.51 /227.51
R ₀ =R ₄₅	50.7200, 5.9210	50.8548, 5.9210	50.7198, 6.1334	0.00/90.00

TABLE V: ET coordinates and azimuths (clockwise from North).

Order \ α	$-3, -2, -1$	$0, \frac{1}{2}, 1, \frac{2}{3}, 2, 3$
1st	(SR) ₄₅	(SR) ₀
2nd	(SR) ₀	(SR) ₄₅
3rd	Δ_{15}	Δ_{15}
4th	Δ_{10}	Δ_{10}
5th	Δ'_{15}	Δ'_{15}
6th	Δ'_{10}	Δ'_{10}

TABLE VI: Ranking of ET configurations from most (1st) to least (6th) sensitive for different spectral indices α for the V-mode SNRs.